Determination of the phase coherence length of $PdCoO_2$ nanostructures by conductance fluctuation analysis

T. Harada,[1,*] P. Bredol,[2] H. Inoue,[1,3] S. Ito,[1] J. Mannhart,[2] and A. Tsukazaki[1,4]

[1]*Institute for Materials Research, Tohoku University, Sendai 980-8577, Japan*

[2]*Max Planck Institute for Solid State Research, Heisenbergstrasse 1, 70569 Stuttgart, Germany*

[3]*Frontier Research Institute for Interdisciplinary Sciences, Tohoku University, Sendai 980-8578, Japan*

[4]*Center for Spintronics Research Network (CSRN), Tohoku University, Sendai 980-8577, Japan*

(Received 24 June 2020; revised 18 December 2020; accepted 21 December 2020; published 19 January 2021)

The two-dimensional layered compound $PdCoO_2$ is one of the most conductive oxides, providing an intriguing research arena opened by the long mean free path and the very high mobility of $\sim 51\,000\,cm^2/V\,s$. These properties turn $PdCoO_2$ into a candidate material for nanoscale quantum devices. By exploring universal conductance fluctuations originating in nanoscale $PdCoO_2$ Hall-bar devices, we determined the phase coherence length of electron transport in c-axis oriented $PdCoO_2$ thin films to equal $\sim$100 nm. The weak temperature dependence of the measured phase coherence length suggests that defect scattering at twin boundaries in the $PdCoO_2$ thin film governs phase breaking. These results suggest that phase coherent devices can be achieved by realizing the devices smaller than the size of twin domains, via refined microfabrication and suppression of twin boundaries.

DOI: 10.1103/PhysRevB.103.045123

Quantum phase coherence in mesoscopic conductors has been intensively studied to explore fundamental questions of quantum mechanics as well as to pursue device architectures [1,2]. The phase coherence length l_ϕ of the charge carriers is the fundamental key parameter governing the quantum interference phenomena in such mesoscopic devices. This coherence length is a measure of the distance over which an electron propagates while maintaining its phase information. The dominant origin of the phase breaking of conducting charges is inelastic scattering provided by electron-electron, electron-phonon, and electron-defect scattering [3]. Information on l_ϕ is obtainable from studies of universal conductance fluctuations (UCFs) as well as other interference effects such as weak (anti)localization and Aharonov-Bohm effect. Here, we focus on a UCF that shows nonperiodic features distinguishable from other effects. In a conductor with a size smaller or comparable to l_ϕ, we can expect the electron interference resulting from travel on different trajectories [γ_n and γ_m in Fig. 1(a)]. Being dependent on interference patterns of electron wave functions, the total conductance of the channel fluctuates due to rearrangement of scattering sources as well as phase shifts induced by magnetic fields [2,4,5]. By analyzing the UCF in magnetoconductance, phase coherence length can be precisely evaluated.

The highly conductive layered metal $PdCoO_2$ has a characteristic anisotropic crystal structure with alternating Pd^+ and $[CoO_2]^-$ layers [Fig. 1(a), left] [6,7]. Whereas the Pd^+ layers mediate the electron conduction [8,9], the $[CoO_2]^-$ layers are of insulating nature, forming quasi-two-dimensional (quasi-2D) electronic systems. In fact, a cylindrical Fermi surface with a nearly hexagonal cross section has been observed by angle-resolved photoemission spectroscopy (ARPES) [10] and the de Haas–van Alphen effect [9]. The closed Fermi surface geometry minimizes the effect of electron-phonon and umklapp scattering processes [9], as is the case in alkaline metals [11]. The high conductivity with the long electron mean free path ($\sim$20 μm) [9,12–14] reported for a bulk single crystal makes $PdCoO_2$ a promising platform for studying quantum transport [15], as the phase coherence length is also expected to be large. As explored in semiconductor heterostructures in the last decades [2], the quantum interference effects have been intensively studied with mesoscopic devices fabricated by a well-regulated growth technique and high-resolution lithography techniques. As for $PdCoO_2$, c-axis oriented thin films have been grown by pulsed-laser deposition (PLD) [16,17], molecular beam epitaxy [18,19], and solid-phase reactions of precursors [20,21]. Establishing a route to pattern $PdCoO_2$ thin films to submicron scales is essential for realizing quantum devices utilizing $PdCoO_2$ thin films and heterostructures. In this study, we report on the determination of the phase coherence length of conducting electrons in mesoscopic Hall-bar devices of $PdCoO_2$ thin films by analyzing the UCF. Based on the autocorrelation analysis of the UCF, we suggest that twin boundaries in the films are one of the dominant scattering sources that cause phase breaking in the $PdCoO_2$ nanostructures.

The c-axis oriented $PdCoO_2$ thin films with the thickness $d = 6.8 \pm 1.5$ nm and 7.0 ± 1.4 nm were grown by PLD on Al_2O_3 (0001) substrates (see Fig. S1 of the Supplemental Material [22]). The thickness d is the average value determined

*Present address: International Center for Materials Nanoarchitectonics, National Institute for Materials Science, Japan; HARADA.Takayuki@nims.go.jp; t.harada@imr.tohoku.ac.jp

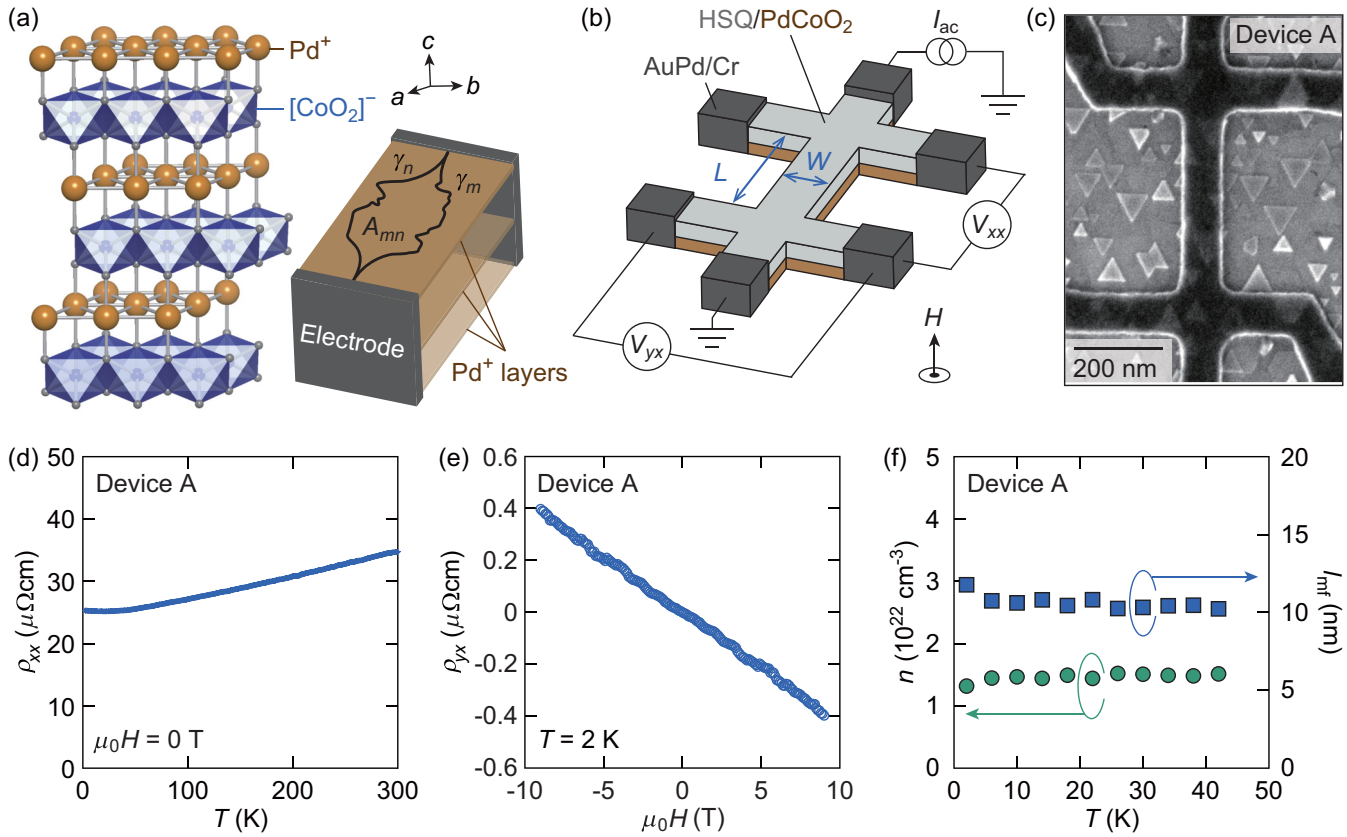

FIG. 1. (a) Left: the crystal structure of $PdCoO_2$. Right: a schematic drawing of $PdCoO_2$ channel with Pd^+ conductive sheets connected to the electrodes. Two trajectories of electrons, γ_n and γ_m, are shown as black curves. The area surrounded by γ_n and γ_m is noted as A_{mn}. Magnetic flux penetrating A_{mn} alters the phase difference of the trajectories γ_n and γ_m. (b) A schematic of a Hall-bar device fabricated on c-Al_2O_3 substrates. The longitudinal (V_{xx}) and transverse voltage (V_{yx}) were measured using the alternating excitation current (I_{ac}) under a magnetic field H applied perpendicular to the $PdCoO_2$ top surface. L and W stand for the separation between the voltage terminals and the width of the channel, respectively. (c) A SEM image of the HSQ resist (dark region) patterned on $PdCoO_2/c$-Al_2O_3 captured before the Ar-ion milling. The triangular patterns of surface morphology were also visible. (d) Resistivity (ρ_{xx}) versus T properties of the Hall-bar device under $\mu_0 H = 0$ T and $I_{ac} = 10$ nA. (e) Hall resistivity (ρ_{yx}) versus $\mu_0 H$ data measured at $T = 2$ K. (f) Temperature dependence of the carrier density (n) (green circles) and the mean free path (l_{mf}) (blue squares) estimated by the Drude model: $l_{mf} = v_F \tau = m^* v_F / n e^2 \rho_{xx}$, where v_F is Fermi velocity, τ is scattering time, m^* is the effective mass of electrons, and e is the elementary charge. We used $m^* = 1.49 m_0$ and $v_F = 7.5 \times 10^5$ ms^{-1} taken from measurements of bulk samples [6].

from the Laue oscillations of the $PdCoO_2$ (0006) peak in the x-ray diffraction (Fig. S1). The errors of d correspond to the root-mean-square roughness of the surface measured by atomic force microscopy (Fig. S2). The $PdCoO_2$ thin films were patterned into mesoscopic Hall-bar devices as shown in Fig. 1(b) using electron-beam lithography and Ar-ion milling [22]. A negative resist composed of hydrogen silsesquioxane (HSQ) was used as a mask for Ar-ion milling. Figure 1(c) shows the scanning electron microscope (SEM) image of the HSQ mask patterned on the $PdCoO_2$ thin film before Ar-ion milling. According to the SEM image, the width W and the length L of the Hall-bar device were estimated to be $W = 93$ nm and $L = 410$ nm, respectively [Figs. 1(b) and 1(c)]. The triangular shapes in Fig. 1(c) are attributed to the surface morphology of the $PdCoO_2$ film [16]. The longitudinal (V_{xx}) and the transverse voltage (V_{yx}) were measured by a lock-in technique using alternating excitation current ($I_{ac} = 10$–500 nA in amplitude). The size of the devices studied in this work is summarized in the Table S1.

The temperature (T) dependence of resistivity ($\rho_{xx} = V_{xx} W d / I_{ac} L$) showed a positive $d\rho_{xx}/dT$ down to $T \sim 50$ K [Fig. 1(d)]. Below ~20 K, the ρ_{xx} slightly increased with decreasing T, approaching asymptotically $\rho_{xx} \propto \ln(1/T)$ (Fig. S3). Such Kondo-like behavior could be due to the surface magnetism of $PdCoO_2$ [23,24]. The linear current-voltage (I-V) characteristics indicates the effect of Joule heating to be negligible for the applied current (<1 μA) (Fig. S4). The Hall resistivity ($\rho_{yx} = V_{yx} d / I_{ac}$) displayed a linear magnetic field (H) dependence with a negative slope, consistent with the electrical conduction being dominated by electron-type charge carriers [10] [Fig. 1(e)]. The carrier density (n) evaluated by the Hall effect measurement was almost constant in the measured temperature range below 42 K, being around $n = 1.5 \times 10^{22}$ cm^{-3} [Fig. 1(f)]. This value is smaller than the bulk value of 2.45×10^{22} cm^{-3} (Ref. [6]). We note that unpatterned, mm-sized thin films showed n in the range of 2–4$\times 10^{22}$ cm^{-3} [24]. The reduced n of the $PdCoO_2$ Hall-bar device might result from the surface roughness and

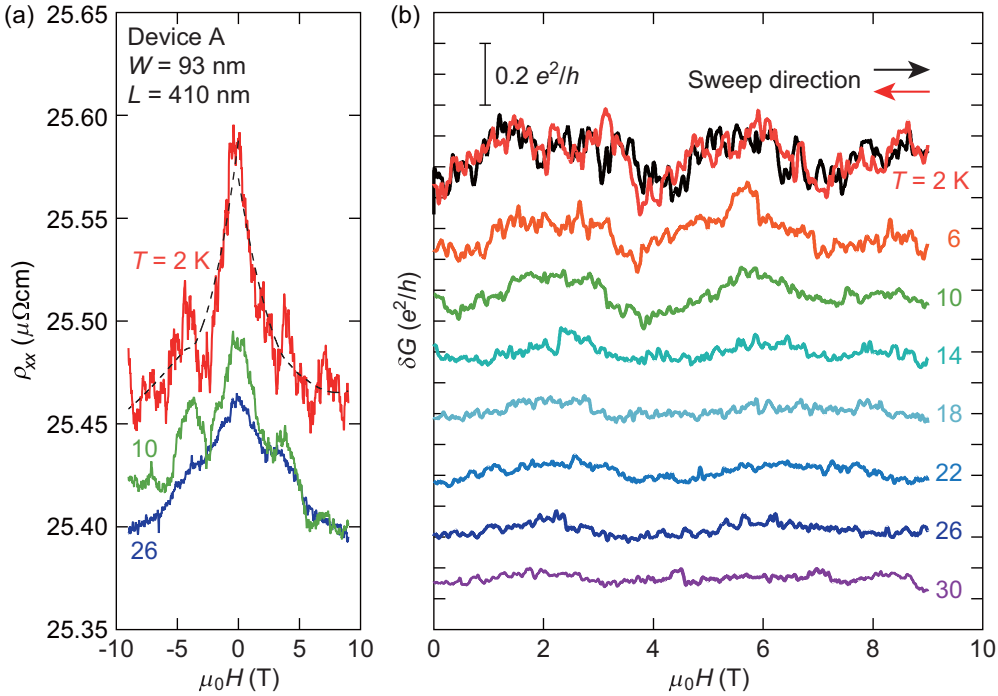

FIG. 2. (a) The measured $\mu_0 H$ dependence of ρ_{xx} at $T = 2$, 10, and 26 K. The amplitude of I_{ac} was set to be $I_{ac} = 500$ nA. The smoothed background (ρ_{xx0}) for $T = 2$ K is shown as the black dashed line. (b) Conductance fluctuation δG obtained by subtracting the smoothed background from the $I_{ac}/V_{xx}(H)$ curves for $T = 2$–30 K. The δG curves are offset along the vertical axis for clarity. The δG of $0.2\,e^2/h$ is shown as a scale for the vertical axis. For $T = 2$ K, two curves measured by sweeping $\mu_0 H$ from 0 to 9 T (black) and from 9 to 0 T (red) are shown. The curves for the other temperatures were measured by sweeping $\mu_0 H$ from 9 to 0 T.

the deviation of the Pd valence state from the bulk value (Pd^+) due to nonideal chemical composition, Ar ion bombardment during patterning, or the effect of surface polarity. The transport mean free path of the electrons (l_{mf}) is readily estimated using the Drude model $l_{mf} = v_F\tau = m^* v_F/ne^2\rho_{xx}$, where v_F is the Fermi velocity, τ is the scattering time, m^* is the effective mass of electrons, and e is the elementary charge [25]. With applying $m^* = 1.49m_0$ and $v_F = 7.5\times10^5$ ms^{-1} as reported for bulk single crystals [6], where m_0 is the mass of rest electrons, the mean free path l_{mf} is estimated to be approximately 10 nm below 42 K as plotted in Fig. 1(f). The l_{mf} of the $PdCoO_2$ thin films explored is much shorter than that of a bulk single crystal ($l_{mf} \sim 21.4\,\mu$m) and coincides with the film thickness. Improving l_{mf} would require achieving better crystalline quality as well as understanding the effect of surface and interface scattering in anisotropic conductors. From the relation $l_{mf} < W$ and L, we conclude that the electron transport in the device is in the diffusive regime as shown in the right schematics of Fig. 1(a).

Under perpendicular magnetic field (H) at $T = 2$ K, the $\rho_{xx}(H)$ dependence shows characteristic fluctuations [Fig. 2(a), red] superposed with the negative magnetoresistance. The amplitude of the fluctuations decreases above $T = 10$ K (green) and vanishes at $T \sim 26$ K (blue). Such fluctuations of ρ_{xx} have been observed in mesoscopic structures of metals [26,27], semiconductors [28–31], graphene [32], and topological insulators [33–35] as a result of quantum interference effects. The amplitude of the fluctuation in the device with $W = 1\,\mu$m and $L = 5\,\mu$m is much smaller than in the device with $W = 93$ nm and $L = 410$ nm (Fig. S5) [22], indicating that the fluctuation originates from mesoscopic phenomena. To analyze the fluctuations quantitatively, the channel conductance $G(T, H) = I_{ac}/V_{xx} = Wd/L\rho_{xx}$ has to be considered. The background $G_0(T, H) = Wd/L\rho_{xx0}$ is subtracted to extract the conductance fluctuation $\delta G = G(T, H) - G_0(T, H)$. Here ρ_{xx0} is the H-dependent smoothed resistivity curve, plotted as a black dashed line for $T = 2$ K in Fig. 2(a). We note that the broad negative magnetoresistance of the smoothed resistivity curve ρ_{xx0} cannot be fitted with the weak localization model, and therefore likely originates from other effects. The δG versus H characteristics, shown in Fig. 2(b), exhibit broad fluctuations with dips around $\mu_0 H = 4$ and 7 T reproducibly from $T = 2$ to 26 K. As shown for $T = 2$ K, the dip features are consistently observed in both sweep directions of the magnetic field [red and black lines in Fig. 2(b)] as well as in different sweeps (Fig. S6), and are therefore not caused by extrinsic random noise. Similar fluctuations have been observed in multiple devices fabricated on different $PdCoO_2$ thin films (Fig. S7).

We analyze the aperiodic fluctuations shown in Fig. 2(b) using the standard UCF model [5,36]. Here, we introduce the autocorrelation function $F(T, \Delta H)$ for δG as

$$F(T, \Delta H) = \langle \delta G(T, H)\delta G(T, H + \Delta H)\rangle_H, \qquad (1)$$

where $\langle ...\rangle_H$ stands for averaging over H. As plotted in Fig. 3, the $F(T, \Delta H)$ dependence changes systematically as the temperature is increased from 2 to 30 K. The correlation field ($\mu_0 H_c$) is evaluated by using the relation $F(T, H_c) = F(T, 0)/2$ (Ref. [36]), as plotted in the inset of Fig. 3. H_c corresponds to a magnetic flux in the phase coherent region of the

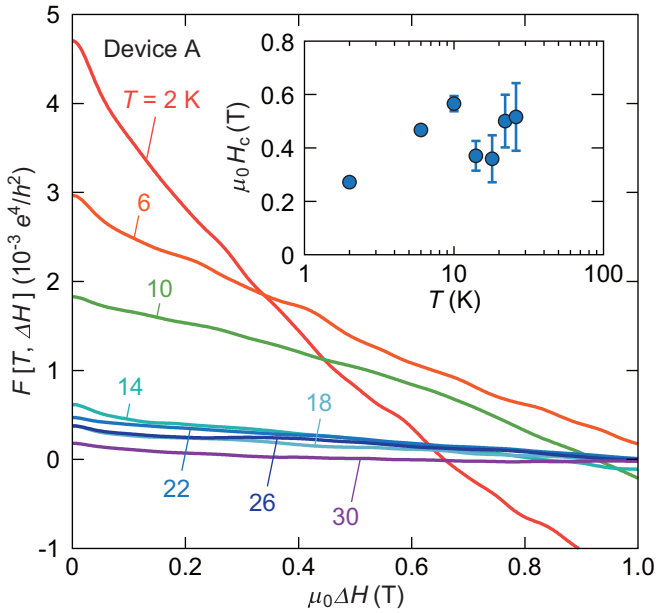

FIG. 3. The autocorrelation function $F(T, \Delta H) = \langle \delta G(T, H)\delta G(T, H + \Delta H)\rangle_H$ plotted as a function of $\mu_0 \Delta H$, obtained from the conductance fluctuations measured at the temperatures noted. The inset displays the temperature dependence of the correlation field H_c. The error bars were calculated by considering the measurement noise that was evaluated from the magnetoconductance curve at $T = 50$ K where the UCF are suppressed (Fig. S11).

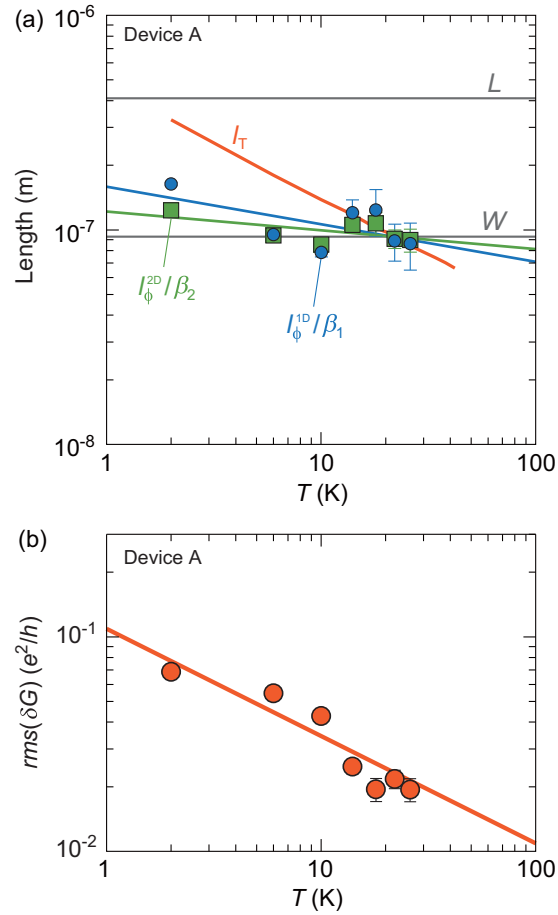

FIG. 4. (a) Temperature dependence of l_ϕ^{1D}/β_1 (blue circles), l_ϕ^{2D}/β_2 (green squares), and the thermal length (l_T) (red line). The thermal length l_T is estimated using $l_T = (hD/k_B T)^{1/2}$. For the calculation of l_T and D, we used the ρ_{xx} and n plotted in Figs. 1(d) and 1(f), respectively. The gray lines correspond to the width W and the length L of the Hall-bar device. The blue and green lines are the linear fitting to l_ϕ^{1D}/β_1 and l_ϕ^{2D}/β_2, respectively. (b) The root-mean-square of the conductance fluctuation $\mathrm{rms}(\delta G) = F[T, 0]^{1/2}$. The red line shows the $T^{-1/2}$ dependence. The error bars are obtained from the measurement noise of the magnetoconductance curve that was evaluated at $T = 50$ K where the UCF are suppressed (Fig. S11).

order of a flux quantum $\phi_0 = h/e$. Thus, the H_c is related to the phase coherence length l_ϕ as $\mu_0 H_c = \beta_1 \phi_0 / W l_\phi$ for one-dimensional (1D) systems ($l_\phi \gg W$) and $\mu_0 H_c = \beta_2 \phi_0 / {l_\phi}^2$ for two-dimensional (2D) systems ($l_\phi \ll W$), where β_1 and β_2 are geometry-dependent constants of order unity [36,37]. The phase coherence length is estimated to be approximately 100 nm at 2–20 K as plotted in Figs. 4(a) and S8. We use the symbols l_ϕ^{1D} and l_ϕ^{2D} to distinguish the phase coherence length estimated by the 1D and 2D models, respectively. As both values of l_ϕ^{1D}/β_1 (blue circles) and l_ϕ^{2D}/β_2 (green squares) are close to the device width W as shown in Fig. 4(a), the dimension of the system is likely in the crossover regime between one and two dimensions. We note that the length L of the Hall-bar device exceeds l_ϕ^{1D}/β_1 and l_ϕ^{2D}/β_2. This indicates that inelastic scattering at its etched sidewalls alone cannot account for l_ϕ^{1D}/β_1 and l_ϕ^{2D}/β_2 being comparable to 100 nm. In disordered 1D and 2D conductors, the dominant cause of phase breaking are electric field fluctuations caused by the motion of the other electrons, also known as electron-electron scattering with small energy transfer or the Nyquist mechanism [3,38]. Although l_ϕ is expected to decay with $T^{-1/3}$ in 1D and $T^{-1/2}$ in 2D systems if phase breaking is mainly subject to the Nyquist mechanism [38], in the $PdCoO_2$ Hall-bar devices, both, l_ϕ^{1D}/β_1 and l_ϕ^{2D}/β_2, do not depend much on T [Figs. 4(a) and S8]. The linear fit of the logarithmic plots yields slopes of -0.18 for l_ϕ^{1D}/β_1 (blue line) and -0.09 for l_ϕ^{2D}/β_2 (green line), the absolute values of which are much smaller than the values predicted by theory (-0.33 and -0.5, respectively). On the other hand, the root mean square (rms) of the conductance fluctuation, calculated as $\mathrm{rms}(\delta G) = \{\langle \delta G^2 \rangle_{\mu_0 H}\}^{1/2} = \{F(T, 0)\}^{1/2}$, decreases with increasing temperature [Fig. 4(b)]. The rms(δG) is proportional to $T^{-1/2}$ dependence (red line) from the largest value of $0.07\, e^2/h$ at $T = 2$ K. Such a temperature dependence of the rms(δG), reproducibly observed in different devices (Fig. S9), often comes from the temperature dependence of l_ϕ [36]. As the l_ϕ^{1D}/β_1 and l_ϕ^{2D}/β_2 are hardly dependent on temperature, however, it is not the phase coherence length that causes the temperature dependence of the rms(δG) of the $PdCoO_2$ Hall-bar device. We therefore interpret the $T^{-1/2}$ dependence of rms(δG) as a thermal averaging effect that is characterized by the thermal length $l_T = (hD/k_B T)^{1/2}$ [Fig. 4(a)], which is comparable to l_ϕ^{1D}/β_1 and l_ϕ^{2D}/β_2. Here, $D = {v_F}^2 \tau/2 = {v_F}^2 m^* {\rho_{xx}}^{-1}/2ne^2$ is the electronic diffusion constant [25,36]. Using $l_\phi \sim 100$ nm and $D \sim 44\,\mathrm{cm}^2/\mathrm{s}$, the phase-breaking time $\tau_\phi = l_\phi^2/D$ is estimated to equal 2 ps at $T = 2$ K.

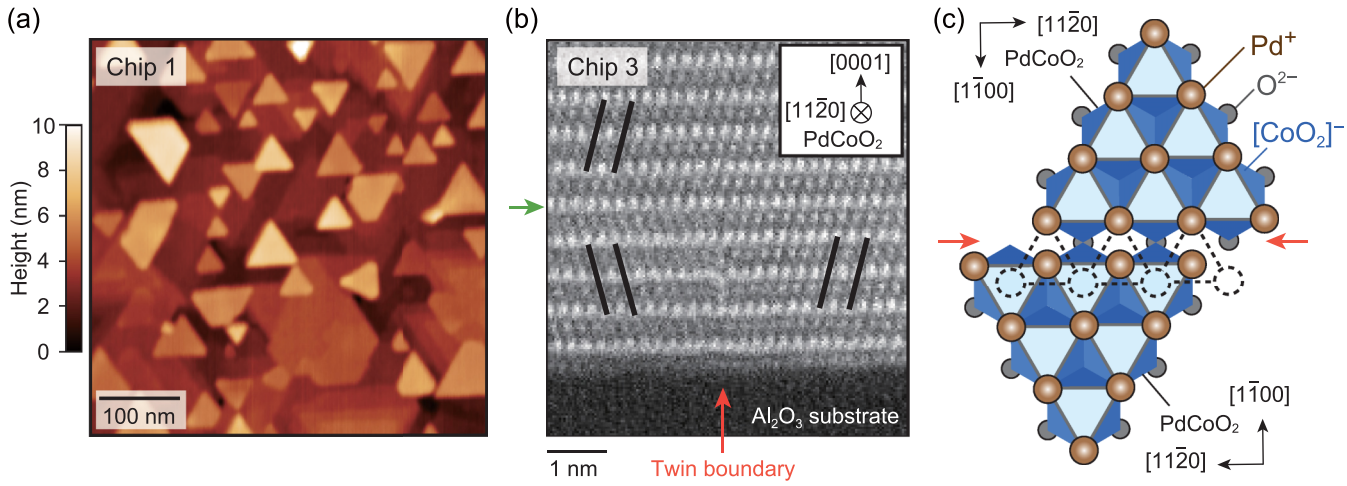

FIG. 5. (a) The AFM image of a $PdCoO_2$ thin film ($d = 6.8 \pm 1.5$ nm) grown on an Al_2O_3 (0001) substrate. (b) The HAADF-STEM image of a $PdCoO_2$ thin film ($d \sim 10$ nm). The twin domains can be classified by the arrangement of the Pd-Co-Pd columns (highlighted with the black lines). A twin boundary and a stacking fault are marked by red and green arrows, respectively. (c) The crystal structure at a twin boundary (red arrows). The black dashed line indicates the positions of Pd atoms of the extended crystal lattice of the upper twin.

It is noteworthy that the evaluated phase coherence length barely changes with temperature. We therefore conclude that the phase breaking is caused by a temperature-independent mechanism, which is likely related to the defects present in the device [39]. The boundaries of the twin domains of the $PdCoO_2$ thin films are candidates for such defects. On Al_2O_3 (0001) substrates, $PdCoO_2$ thin films grow with 180 °-rotated crystal twins [16]. The trigonal crystal structure of $PdCoO_2$ results in the triangular step-and-terrace structure seen in Fig. 5(a) which comprises two kinds of triangular structures that are 180 °-rotated from each other. The steps with a-few-nm height provide for the rms roughness of ∼1.5 nm (see Figs. S2 and S10). The orientations of triangular step-and-terrace structures [Figs. 5(a) and S2] can depend on the in-plane orientation of 180 °-rotated crystal twins [16] and/or the surface energy of the growing domains. To therefore analyze the twin boundaries in the $PdCoO_2$ samples, we applied high-angle annular dark-field scanning transmission electron microscope (HAADF-STEM) [Fig. 5(b)]. The whiteish dots in Fig. 5(b) correspond to the Pd atoms with the large atomic number in the *Z*-contrast image. The layered structure in the image reflects the *c*-axis orientation of the film. Regarding the orientations in the *ab* plane, we can classify twin domains by the resulting difference of the lattice arrangements along the Pd-Co-Pd columns highlighted with black lines. There are twin boundaries (red arrow) and stacking faults (green arrow) caused by the twinning. Considering the quasi-2D conduction properties of $PdCoO_2$ [9], the twin boundaries as indicated by the red arrow mainly influence the in-plane conduction. Although it is difficult to detect multiple twin boundaries in one micrograph, we can determine the minimum distance of the twin boundaries in our experiment to equal at least 40 nm. The density of the twin boundaries is therefore in the range to account for the l_ϕ^{1D}/β_1 and l_ϕ^{2D}/β_2 of about 100 nm [Fig. 4(a)].

The periodicity of the Pd lattice at the twin boundaries is schematically depicted in Fig. 5(c). As shown by the upper triangle, the expected Pd sites (black dashed line) of the upper domains are located at the interstitial sites of the other twin. Thus, the twin boundaries can be regarded as planes consisting of interstitial Pd atoms and/or Pd vacancies. Such planes induce electron scattering. Internal degrees of freedom such as vibrations of the interstitial Pd atoms at the twin boundaries may scatter electrons inelastically. Indeed, Frenkel pairs, i.e., combinations of an interstitial Pd and a Pd vacancy, were reported to significantly increase the resistivity of $PdCoO_2$ single crystals [40]. The large coherence length within the domains can be bounded by the inelastic scattering at the twin boundaries, where a slight mismatch of the Fermi surface between the twins requires a change of the incident electron momentum. The disappearance of conductance fluctuations above 26 K is explained by l_T becoming sufficiently shorter than the phase coherence length that is bounded by the Hall-bar width and the size of twin domains (>40 nm) [Fig. 4(a)]. According to these considerations, the twin boundaries are likely the dominant cause of phase breaking in the $PdCoO_2$ thin film.

In summary, we have measured the electrical transport properties of a submicron-scale Hall-bar device of a $PdCoO_2$ thin film. Universal conductance fluctuations are found in magnetoresistance at temperatures below 26 K. By applying an autocorrelation analysis, the phase coherence length of the electrons in the $PdCoO_2$ Hall-bar device is found to equal ∼100 nm at 2 K. The phase breaking length is proposed to be limited by the existence of crystal twin boundaries that cause phase-breaking scattering of the conduction electrons. This demonstration of quantum coherence in a $PdCoO_2$ nanostructure is a first step to study the interplay of quantum transport and the exotic properties caused by the high conductivity [13,14] and the polar surface [23,24,41] of $PdCoO_2$ in thin-film mesoscopic devices. According to our results, the suppression of twin boundaries is essential for further extending the phase coherence length. Such suppression may be possible by use of delafossite-type substrates [42] with optimized miscut angles [17] to lift the degeneracy of the formation energy of twins.

We thank K. Fujiwara for valuable comments on the manuscript. This work was a cooperative program (Proposal No. 18G0407) of the CRDAM-IMR, Tohoku University. This work was partly supported by a Grant-in-Aid for Early-Career Scientists (Grants No. 18K14121 and No. 19K23415) from the Japan Society for the Promotion of Science (JSPS) and JST CREST (Grant No. JPMJCR18T2), JST, PRESTO (Grant No. JPMJPR20AD), Mayekawa Houonkai Foundation, Tanaka Kikinzoku Memorial Foundation, and Grant for Basic Science Research Projects from The Sumitomo Foundation.

[1] T. Ihn, *Semiconductor Nanostructures: Quantum States and Electronic Transport* (Oxford University Press, New York, 2009).
[2] C. W. J. Beenakker and H. van Houten, *Quantum Transport in Semiconductor Nanostructures* (Academic Press, New York, 1991).
[3] J. J. Lin and J. P. Bird, J. Phys.: Condens. Matter **14**, R501 (2002).
[4] B. L. Al'tshuler, V. E. Kravtsov, and I. V. Lerner, Pis'ma Zh. Eksp. Teor. Fiz. **43**, 342 (1986) [JETP Lett. **43**, 441 (1986)].
[5] P. A. Lee and A. D. Stone, Phys. Rev. Lett. **55**, 1622 (1985).
[6] A. P. Mackenzie, Rep. Prog. Phys. **80**, 032501 (2017).
[7] R. Daou, R. Frésard, V. Eyert, S. Hébert, and A. Maignan, Sci. Technol. Adv. Mater. **18**, 919 (2017).
[8] T. Higuchi, T. Tsukamoto, M. Tanaka, H. Ishii, K. Kanai, Y. Tezuka, S. Shin, and H. Takei, J. Electron. Spectrosc. Relat. Phenom. **92**, 71 (1998).
[9] C. W. Hicks, A. S. Gibbs, A. P. Mackenzie, H. Takatsu, Y. Maeno, and E. A. Yelland, Phys. Rev. Lett. **109**, 116401 (2012).
[10] H.-J. Noh, J. Jeong, J. Jeong, E.-J. Cho, S. B. Kim, K. Kim, B. I. Min, and H.-D. Kim, Phys. Rev. Lett. **102**, 256404 (2009).
[11] M. Kaveh and N. Wiser, Adv. Phys. **33**, 257 (1984).
[12] H. Takatsu, S. Yonezawa, S. Mouri, S. Nakatsuji, K. Tanaka, and Y. Maeno, J. Phys. Soc. Jpn. **76**, 104701 (2007).
[13] P. J. W. Moll, P. Kushwaha, N. Nandi, B. Schmidt, and A. P. Mackenzie, Science **351**, 1061 (2016).
[14] M. D. Bachmann, A. L. Sharpe, A. W. Barnard, C. Putzke, M. König, S. Khim, D. Goldhaber-Gordon, A. P. Mackenzie, and P. J. W. Moll, Nat. Commun. **10**, 5081 (2019).
[15] C. Putzke, M. D. Bachmann, P. McGuinness, E. Zhakina, V. Sunko, M. Konczykowski, T. Oka, R. Moessner, A. Stern, M. König, S. Khim, A. P. Mackenzie, and P. J. W. Moll, Science **368**, 1234 (2020).
[16] T. Harada, K. Fujiwara, and A. Tsukazaki, APL Mater. **6**, 046107 (2018).
[17] P. Yordanov, W. Sigle, P. Kaya, M. E. Gruner, R. Pentcheva, B. Keimer, and H.-U. Habermeier, Phys. Rev. Mater. **3**, 085403 (2019).
[18] M. Brahlek, G. Rimal, J. M. Ok, D. Mukherjee, A. R. Mazza, Q. Lu, H. N. Lee, T. Z. Ward, R. R. Unocic, G. Eres, and S. Oh, Phys. Rev. Mater. **3**, 093401 (2019).
[19] J. Sun, M. R. Barone, C. S. Chang, M. E. Holtz, H. Paik, J. Schubert, D. A. Muller, and D. G. Schlom, APL Mater. **7**, 121112 (2019).
[20] P. F. Carcia, R. D. Shannon, P. E. Bierstedt, and R. B. Flippen, J. Electrochem. Soc. **127**, 1974 (1980).
[21] R. Wei, P. Gong, M. Zhao, H. Tong, X. Tang, L. Hu, J. Yang, W. Song, X. Zhu, and Y. Sun, Adv. Funct. Mater. **30**, 2002375 (2020).
[22] See Supplemental Material at http://link.aps.org/supplemental/10.1103/PhysRevB.103.045123 for detailed information.
[23] F. Mazzola, V. Sunko, S. Khim, H. Rosner, P. Kushwaha, O. J. Clark, L. Bawden, I. Marković, T. K. Kim, M. Hoesch, A. P. Mackenzie, and P. D. C. King, Proc. Natl. Acad. Sci. USA **115**, 12956 (2018).
[24] T. Harada, K. Sugawara, K. Fujiwara, M. Kitamura, S. Ito, T. Nojima, K. Horiba, H. Kumigashira, T. Takahashi, T. Sato, and A. Tsukazaki, Phys. Rev. Res. **2**, 013282 (2020).
[25] N. W. Ashcroft and N. D. Mermin, *Solid State Physics* (Thomson Learning, Inc., Boston, 1976).
[26] C. P. Umbach, S. Washburn, R. B. Laibowitz, and R. A. Webb, Phys. Rev. B **30**, 4048 (1984).
[27] J. S. Moon, N. O. Birge, and B. Golding, Phys. Rev. B **56**, 15124 (1997).
[28] S. B. Kaplan and A. Hartstein, Phys. Rev. Lett. **56**, 2403 (1986).
[29] D. Stornaiuolo, S. Gariglio, N. J. G. Couto, A. Fête, A. D. Caviglia, G. Seyfarth, D. Jaccard, A. F. Morpurgo, and J.-M. Triscone, Appl. Phys. Lett. **101**, 222601 (2012).
[30] C. Blömers, M. I. Lepsa, M. Luysberg, D. Grützmacher, H. Lüth, and T. Schäpers, Nano Lett. **11**, 3550 (2011).
[31] R. P. Taylor, M. L. Leadbeater, G. P. Whittington, P. C. Main, L. Eaves, S. P. Beaumont, I. McIntyre, S. Thoms, and C. D. W. Wilkinson, Surf. Sci. **196**, 52 (1988).
[32] C. Ojeda-Aristizabal, M. Monteverde, R. Weil, M. Ferrier, S. Guéron, and H. Bouchiat, Phys. Rev. Lett. **104**, 186802 (2010).
[33] J. G. Checkelsky, Y. S. Hor, M.-H. Liu, D.-X. Qu, R. J. Cava, and N. P. Ong, Phys. Rev. Lett. **103**, 246601 (2009).
[34] J. Lee, J. Park, J.-H. Lee, J. S. Kim, and H.-J. Lee, Phys. Rev. B **86**, 245321 (2012).
[35] S. Matsuo, T. Koyama, K. Shimamura, T. Arakawa, Y. Nishihara, D. Chiba, K. Kobayashi, T. Ono, C.-Z. Chang, K. He, X.-C. Ma, and Q.-K. Xue, Phys. Rev. B **85**, 075440 (2012).
[36] P. A. Lee, A. D. Stone, and H. Fukuyama, Phys. Rev. B **35**, 1039 (1987).
[37] V. Chandrasekhar, P. Santhanam, and D. E. Prober, Phys. Rev. B **44**, 11203 (1991).
[38] B. L. Altshuler, A. G. Aronov, and D. E. Khmelnitsky, J. Phys. C: Solid State Phys. **15**, 7367 (1982).
[39] C. Enss and S. Hunklinger, *Low-Temperature Physics* (Springer-Verlag, Heidelberg, 2005).
[40] V. Sunko, P. H. McGuinness, C. S. Chang, E. Zhakina, S. Khim, C. E. Dreyer, M. Konczykowski, H. Borrmann, P. J. W. Moll, M. König, D. A. Muller, and A. P. Mackenzie, Phys. Rev. X **10**, 021018 (2020).
[41] V. Sunko, H. Rosner, P. Kushwaha, S. Khim, F. Mazzola, L. Bawden, O. J. Clark, J. M. Riley, D. Kasinathan, M. W. Haverkort, T. K. Kim, M. Hoesch, J. Fujii, I. Vobornik, A. P. Mackenzie, and P. D. C. King, Nature (London) **549**, 492 (2017).
[42] N. Wolff, T. Schwaigert, D. Siche, D. G. Schlom, and D. Klimm, J. Cryst. Growth **532**, 125426 (2020).